The structures of frataxin oligomers reveal the mechanism for the delivery and detoxification of iron

Karlberg, Tobias; Schagerlöf, Ulrika; Gakh, Oleksandr; Park, Sungjo; Ryde, Ulf; Lindahl, Martin; Leath, Kirstin; Garman, Elspeth; Isaya, Grazia; Al-Karadaghi, Salam

Published in:
Structure

DOI:
10.1016/j.str.2006.08.010

2006

Document Version:
Peer reviewed version (aka post-print)

Frataxin trimer: A novel molecular design for the delivery or detoxification of iron

Tobias Karlberg[1], Ulrika Schagerlöf[1], Oleksandr Gakh[2], Sungjo Park[2], Ulf Ryde[3], Martin Lindahl[1], Grazia Isaya[2*] and Salam Al-Karadaghi[1*]

Departments of [1]Molecular Biophysics and [3]Theoretical Chemistry, Centre for Chemistry and Chemical Engineering, Lund University, P.O. Box 124, SE-221 00 Lund, Sweden.

[2]Departments of Pediatric & Adolescent Medicine and Biochemistry & Molecular Biology, Mayo Clinic College of Medicine, Rochester, MN 55905, U.S.A.

[*]To whom correspondence should be addressed.

E-mail: isaya@mayo.edu, Salam.Al-Karadaghi@mbfys.lu.se

Frataxin performs key functions in iron delivery and detoxification via a currently unknown mechanism. Here we present the crystal structure of frataxin trimer and single particle reconstruction of a 24-subunit oligomer. The trimer has a central funnel-shaped channel where iron binds. The structues provide a framework for understading the function of frataxin in promoting both delivery and detoxification of Fe(II), a combination of roles not found in other known iron-binding proteins. Two conformations with different metal binding energies are observed for the central channel, suggesting that a gated mechanism controls the function of frataxin in iron delivery or storage.

To maintain a vital supply of iron, cells must overcome its limited solubility and propensity to catalize radical reactions (*1*). The mitochondrial protein frataxin can either provide Fe(II) to other proteins (*2-4*) or convert redox-active Fe(II) to a stable Fe(III) mineral (*5*), suggesting a novel mechanism to counteract both the poor availability and the potential toxicity of iron. This mechanism has remained elusive in spite of the avilable three-dimensional structures of monomers of human and yeast frataxin and the bacterial homologue CyaY (*6-8*). Because biochemical evidence had suggested that self-assembly is an important aspect of the frataxin mechanism (*9, 10*), we screened for point mutations that would enable yeast frataxin monomer to self-assemble in a stable manner. A mutant protein in which a conserved tyrosine was replaced with an alanine residue (Y73A) assembled during expression in *E. coli* and was purified in two forms, trimer and a 24-subunit oligomer, which were characterized by X-ray crystallography and single particle electron microscopy reconstruction, respectively.

The trimer is almost flat with overall dimensions of 75 Å × 75 Å × 30 Å (Fig. 1). Each subunit of the trimer is folded into an α/β sandwich with two α–helices (α2, α3) packed against a 5-stranded (β1- β5) anti-parallel twisted β-sheet. Two additional β-strands (β6, β7) build up a β-hairpin which is almost perpendicular to strand β5. A short helix at the protein N-terminus (α1), together with a 7-residue extended coil region connected to helix α2, build up an N-terminal extension (Fig. 1). A comparison with the structure of the yeast or human frataxin monomer (*6, 8*) shows that formation of trimer results in unfolding of helix α2, which is about two turns shorter in the trimer (Fig. S1).

The arrangement of the monomers in the trimer is such that the plane of the β-sheet is inclined with an angle of about 30° relative to the plane of the trimer. Solvent accessible parts of helix α3 and strand β7, the hairpin loop between strands β6 and β7, and the loop between strands β5 and β6 create one surface of the trimer (Fig. 1A). The opposite surface is created by structural elements from two different monomers with the N-terminal extension of one monomer packed against the β-sheet surface of the next monomer, which in turn contributes helix α2, strands β1- β3, and the loop between β3 and β4 to the surface (Fig. 1B). The N-terminal extension is anchored to the core structure at the base (Fig. 1B, Fig. S2A) and through helix α1 (Fig. 1B, Fig. S2B), and appears to play a crucial role in the stabilization of the trimer.

The trimer is further stabilized by interactions between the loops around the 3-fold axis. At one side of the trimer, the β-hairpin loop between strands β6 and β7 (residues S151-G155), the C-terminus of strand β5, and the loop between strands β5 and β6 (residues L144-W149) build up a unique helical structural element (Fig. 2A). Three such

elements are arranged around the three-fold axis of the trimer with the loop between strands β5 and β6 of one monomer packed against the hairpin loop of the next monomer. Two hydrogen bonds between monomers, one between the carbonyl oxygen of L152 and amide group of G147, and the other between the side chain of N146 and the carbonyl of Q154, contribute to the stabilization of the loops (Fig. 2A). The side chains of L145, V150 and L152 from the three monomers are exposed to the solvent and together create a hydrophobic wall at the channel opening (Fig. 2A). In the sequence of human frataxin, Leu145, which is closer to the surface, is exchanged by a threonine while the valine is conserved (Fig. S3).

Three invariant aspartate residues at the end of strand β5 (D143) are located in the middle of the channel with their side chains directed towards the opening at the opposite end of the channel (Fig. 2A, 2B). This opening is built up by residues from the region between G117 and D143, which includes strands β3, β4 and β5 (Fig. 2B), the most highly conserved stretch of amino acids within eukaryotic frataxin sequences (Fig. S3). Residues K123-I130 build up part of strands β3 and β4 and the loop between them. The strands are sharply bent by ~80º relative to the plane of the central β-sheet, while the loop between them (residues P125-K128) extends into the opening of the channel. D143 contributes to the stabilization of the loop conformation by a hydrogen bond to the amide of Q129 of the same monomer, while the side chain of Q129 makes a bond with the carbonyl oxygen of P126 of the next monomer; two additional hydrogen bonds involves the side chain of the next residue in the loop, N127 of one monomer and E75 together with E76 of another (Fig. 2B). Residues P126 and Q129 are among the invariant amino acids in all frataxin sequences (Fig. S3).

Loop P125-K128 can also exist in an alternative conformation in which a flip to the opposite direction (~8 Å) brings the tip of the loop (N127 and Q129) in contact with the opposite monomer (Fig. 2C). New hydrogen bonds are formed between N127 and Q129, and between D143 and the side chains of N127 and Q129 of the same monomer. The hydrogen bonds between N127 and E75 and Q129 and P126 are absent in this conformation. The peptide unit of P126 is flipped, resulting in the carbonyl oxygen pointing in the opposite direction, towards the interior of the channel and towards the side chain of D143 (Fig. 2C). The switch between two conformations may be controlled by interactions with iron or other proteins or by the oligomerization state of frataxin.

The channel is funnel-shaped with openings of ~15 Å and ~4 Å (Fig. 3A, 3B) and increasing acidity toward the smaller opening (Fig. 3C). In analogy with the channels at the 3-fold axis of ferritin shells (*11-13*), the larger and smaller openings may serve as entrance and exit, respectively, for iron ions. However, while the entrance to the ferritin channel is lined up by basic residues, that of the frataxin channel is hydrophobic (Fig. 2A), which may serve to not only guide ions into the channel but also provide a docking surface for other proteins. The X-ray structure of iron-loaded frataxin trimer shows that an iron hydrated by 3 solvent molecules does indeed bind inside the channel close to the suggested entrance at ~4 Å from the side chains of the invariant D143 (Fig. 3C). It can not be excluded that additional solvent molecules, not visible at the present resolution of the data, bridge the interactions between the iron and protein groups. In the iron-bound trimer structure the loop at the presumed channel exit is in the first of the two conformations described above (Fig. 2C). Theoretical estimation shows that in the first conformation the metal binds with an energy which is 2.5 times lower than the binding

energy in the second conformation (-40 and -100 kJ/mol, respectively, Fig. S2C). It is possible that iron binding stabilizes the first conformation, while the second conformation (with higher metal binding energy) is only induced in the presence of metal and additional factors, e.g. by the association of trimers into higher order oligomers. The two states of the channel may reflect the two functions of frataxin: Iron delivery in the trimer (with lower iron binding energy), and iron storage in larger oligomers, which may have higher iron binding energy and higher iron flux through the channel.

Interestingly, the proposed channel exit appears to be connected to negatively charged patches on the side of each monomer (Fig. 3B). The residues forming the acidic patch from the center of the trimer to the sides of each monomer, D78, D79, D82, D86, E89, E90, E93 from helix α2, and D101 and D103 from strand β1, are conserved in eukaryotic sequences (Fig. S3). Biochemical studies have shown that they comprise functionally distinct sites involved in iron oxidation and mineralization (*14*). The patch is lined up by hydrophobic and positively charged residues (H74, H106, K123 and K128). This architecture may serve in leading the metal ion from the potential channel exit to oxidation and mineralization sites for detoxification (*14*). In close vicinity of the channel exit there is a negatively charged surface grove with an arrangement of residues (H74, D79, D82, H83 and D86) reminiscent of the di-iron site in ribonucleotide reductase (*15*) (Fig. 3D). We suggest that this site may serve as the iron oxidation site of frataxin (*14*). The residues constituting the site have a different arrangement in the monomer structure of yeast frataxin (*8*), suggesting that trimer formation is needed for the formation of the oxidation site in agreement with previous biochemical studies (*16*).

In the wild type protein, iron binding likely leads to a conformational change in the N-terminal extension that promotes trimer formation. The Y73A mutation probably induces a conformation of the N-terminal extension that can promote trimer formation even in the absence of iron. Interestingly, soaking of the crystals of iron-free trimer with Co^{2+} identified an additional metal binding site in helix α1 at ~2-2.5 Å from the backbone carbonyl of Leu68 (Fig. 1B and S2B**)**. From its location at the base of the N-terminal extension, it is possible that this metal binding site further regulates the conformation of the N-terminal extension and thus trimer formation.

Reconstruction of the 24-subunit oligomer shows a cubic shape in which trimer represents the basic structural unit, with the center of each trimer positioned at the threefold axis of the cube (Fig. 4A, 4B). Docking of the trimer into the EM reconstruction shows that the particle is primarily stabilized by interactions of the N-terminus of neighboring trimers (Fig. 4C). In addition, the best fit is obtained with the N-termini of the trimers pointing towards the interior of the complex. This location of the N-termus is similar to that observed in ferritin olygomers. It also places the suggested entrance to the channel at the 3-fold axis of each trimer on the outside of the particle, while the exit and the the oxidation and mineralization sites are located in the interior. This is in agreement with the iron storage function of frataxin (*5*), which in large extent seems to follow a mechanism that is similar to that of ferritin (*11*).

The presented trimer structure provides a structural basis for understanding assembly of frataxin and the interplay between frataxin and other proteins. It also provides a framework to dissect how frataxin carries out its function in promoting both the delivery to different targets and the detoxification of Fe(II), a combination of critical

biological roles not found in other known iron-binding proteins. Since the trimer seems to exhibit structural details consistent with both such roles, we propose that it represents the primary functional unit of frataxin. Moreover, the structure for the first time suggests that compounds that would stabilize the frataxin trimer may provide means to maximize frataxin function in individuals affected by frataxin deficiency (*17*). The structure of the trimer can be used for a rational design of such compounds.

References and Notes

1. B. Halliwell, J. M. C. Gutteridge, in *Free radicals in biology and medicine*. (Oxford University Press, 1999) pp. 48-82.
2. A. L. Bulteau *et al.*, *Science* **305**, 242 (2004).
3. S. Park *et al.*, *J Biol Chem* **278**, 31340 (2003).
4. T. Yoon, J. A. Cowan, *J Am Chem Soc* **125**, 6078 (2003).
5. H. Nichol *et al.*, *Biochemistry* **42**, 5971 (2003).
6. S. Dhe-Paganon, R. Shigeta, Y. I. Chi, M. Ristow, S. E. Shoelson, *J Biol Chem* **275**, 30753 (2000).
7. S. J. Cho *et al.*, *Proc Natl Acad Sci U S A* **97**, 8932 (2000).
8. Y. He *et al.*, *Biochemistry* **43**, 16254 (2004).
9. J. Adamec *et al.*, *Am J Hum Genet* **67**, 549 (2000).
10. F. Bou-Abdallah, S. Adinolfi, A. Pastore, T. M. Laue, N. D. Chasteen, *J Mol Biol* **341**, 605 (2004).
11. P. D. Hempstead *et al.*, *FEBS Lett* **350**, 258 (1994).
12. R. A. Grant, D. J. Filman, S. E. Finkel, R. Kolter, J. M. Hogle, *Nat Struct Biol* **5**, 294 (1998).
13. T. J. Stillman *et al.*, *J Mol Biol* **307**, 587 (2001).
14. O. Gakh *et al.*, *Hum Mol Genet* **15**, 467 (2006).
15. P. Nordlund, H. Eklund, *Curr Opin Struct Biol* **5**, 758 (1995).
16. S. Park, O. Gakh, S. M. Mooney, G. Isaya, *J Biol Chem* **277**, 38589 (2002).
17. V. Campuzano *et al.*, *Science* **271**, 1423 (1996).
18. M. Cossee *et al.*, *Ann Neurol* **45**, 200 (1999).

19. All figures were generated with the PyMOL Molecular Graphics System (2002) Delano Scientific, San Carlos, CA, U.S.A.

20. We acknowledge MAX-lab and ESRF for provision of synchrotron radiation facilities and the nCHREM electron bio-microscopy unit. This work was supported by grants from the Swedish Research Council to SAK, and from the NIH/NIA (AG15709) and the Friedreich Ataxia Research Alliance (FARA) to GI.

Supporting Online Material

www.sciencemag.org

Materials and Methods

Table 1, Figs. S1-S5

Supporting References

FIGURE LEGENDS

Fig. 1. Overall architecture of yeast frataxin trimer in ribbon representation. (**A**) Suggested outer surface of the trimer with the exposed helices α2 and α3 (shown in green). Loops are shown in brown and β-strands in blue. Spheres show cobalt ions bound to helix α1. (**B**) Suggested inner surface of the trimer. The N-terminal extension with helix α1 packed against the β-sheet is shown in yellow. Also shown are the side chains of 4 amino acids (P100, G107, W131 and R141) mutation of which (D122Y, G130V, W155R and R165C, human numbering) have been linked to the neurodegenerative disease Friedreich ataxia (*18*). The mutations are predicted to destabilize the trimeric complex (Fig. S5).

Fig. 2. Stereo view of the **s**tructure of the central channel. (**A**) Suggested channel entrance. The helical structural motif from each monomer is shown in gold. **(B)** The first conformation of the proposed channel exit. The primary invariant residues which contribute to the structure and stabilization of the trimer are shown as sticks. **(C)** The second conformation of the proposed channel exit. Purple model with amino acid side chains (shown as sticks) represents the second conformation of the channel exit; for comparison the structure of the first conformation (Fig. 2B) has been superimposed (green ribbon model) demonstrating the position of the loop in the first conformation.

Fig. 3. Potential functional sites and metal binding. (**A-B**) Electrostatic surface potential distribution for the suggested outer (**A**) and inner (**B**) surface of the frataxin trimer. Red and blue denote negative and positive potential, respectively. The residues constituting

one of the three potential ferroxidation sites are shown as sticks. (**C**) Cross section through the central channel showing the electrostatic potential distribution within the channel. The bound iron is shown as a green sphere and solvent molecules as blue spheres. (**D**) The potential ferroxidation site of frataxin viewed with an electrostatic potential surface. Distances (Å) between the side chains are indicated on the figure.

Fig. 4. Electron microscopic model of a 24-subunit frataxin oligomer (reconstructed from 4,000 particles). A total of 8 trimers make the oligomer. (**A**) View approximately along the two fold axis, which relates 2 trimers. (**B**) Packing of trimers docked into the electron microscopy reconstruction. The trimers (green and and purple) are shown in surface representation. (**C**) A stereo view showing interactions between the N-terminal extensions of two trimers packed within the 24-subiunit particle.

Word count: 2726

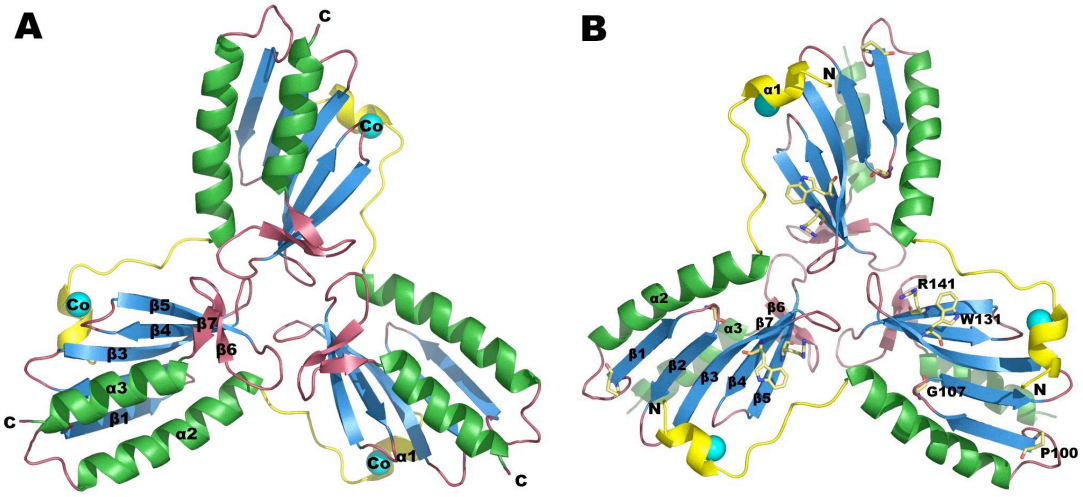

Karlberg et al., Fig. 1

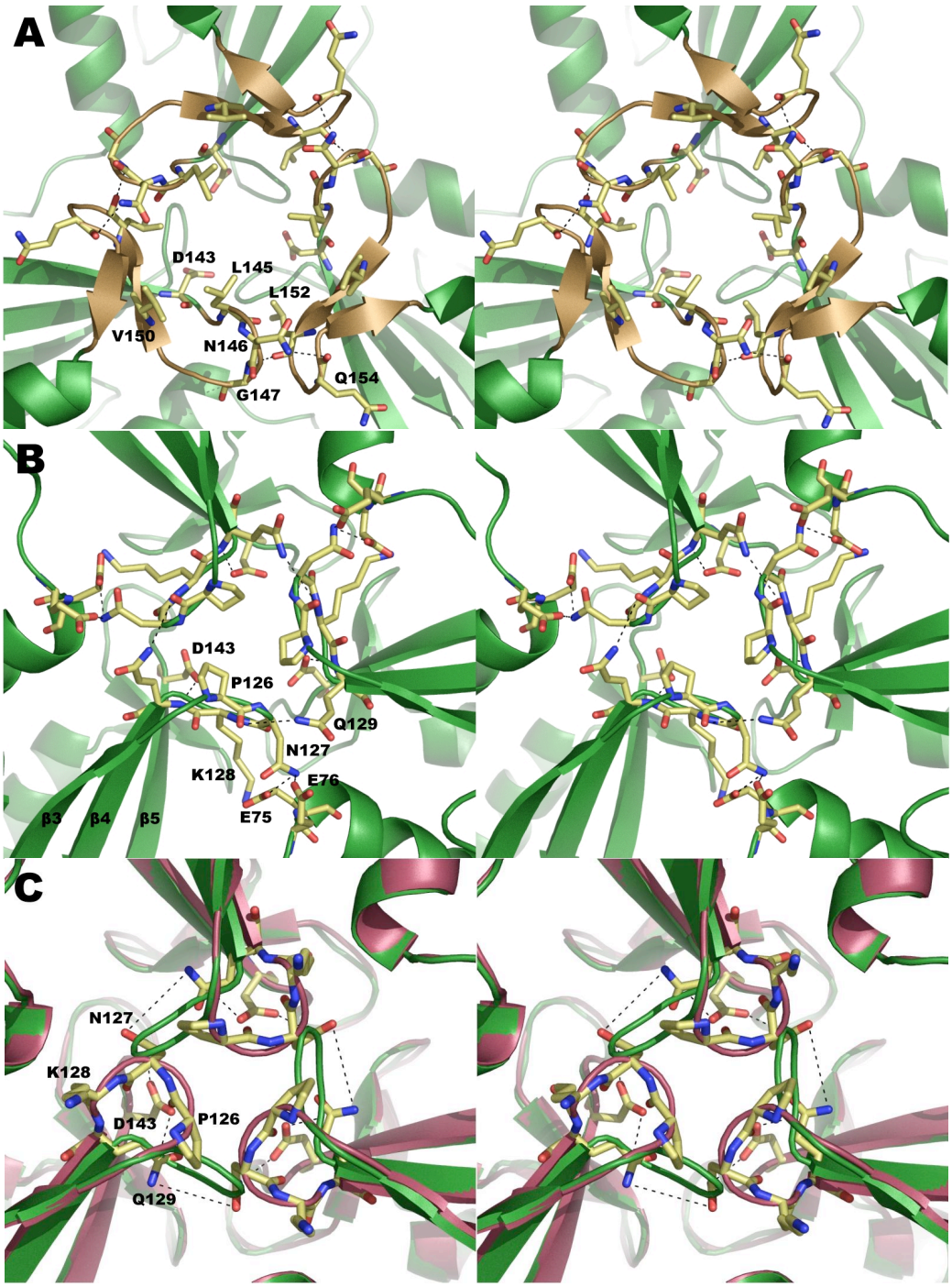

Karlberg et al, Fig. 2

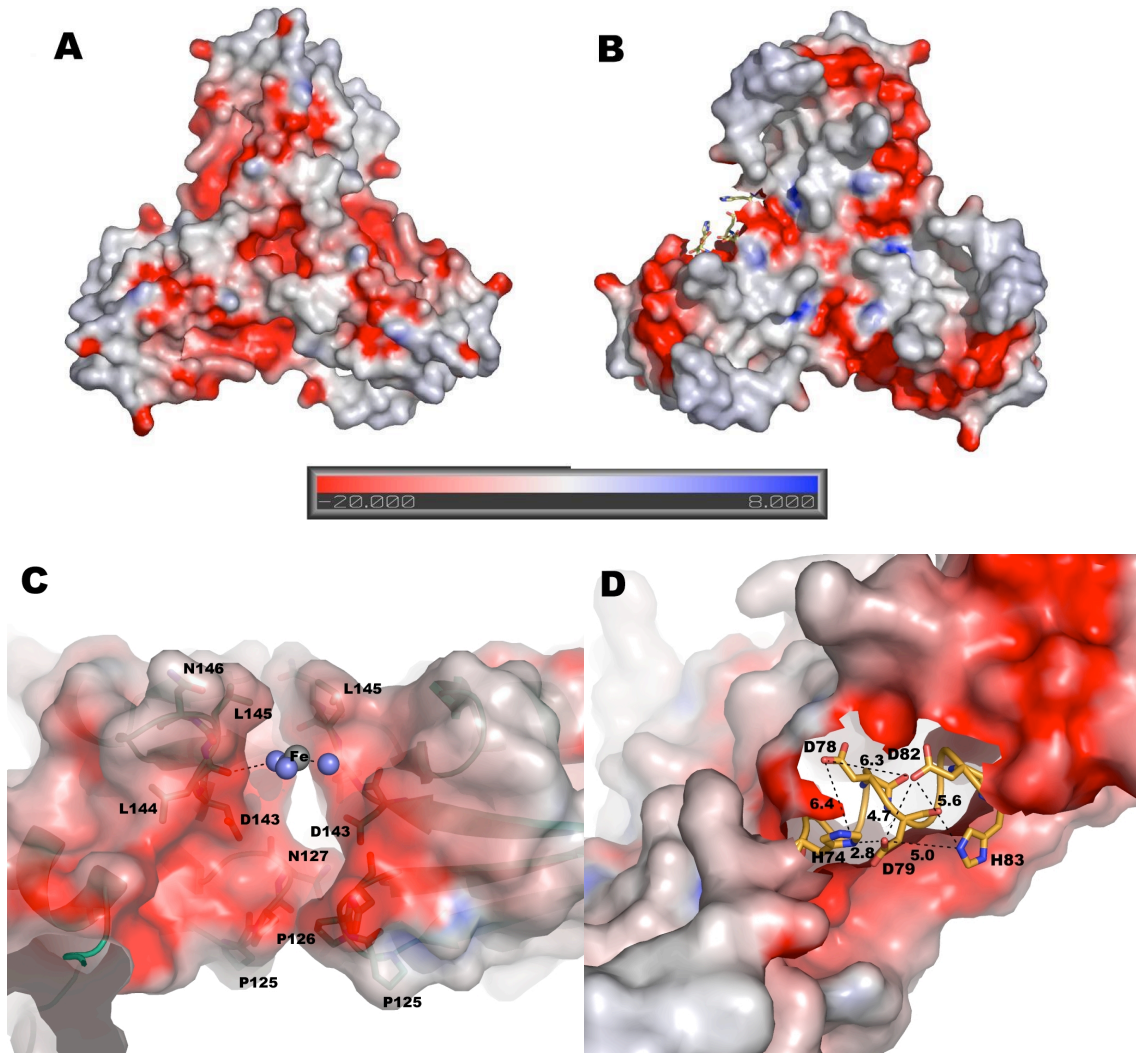

Karlberg et al, Fig. 3

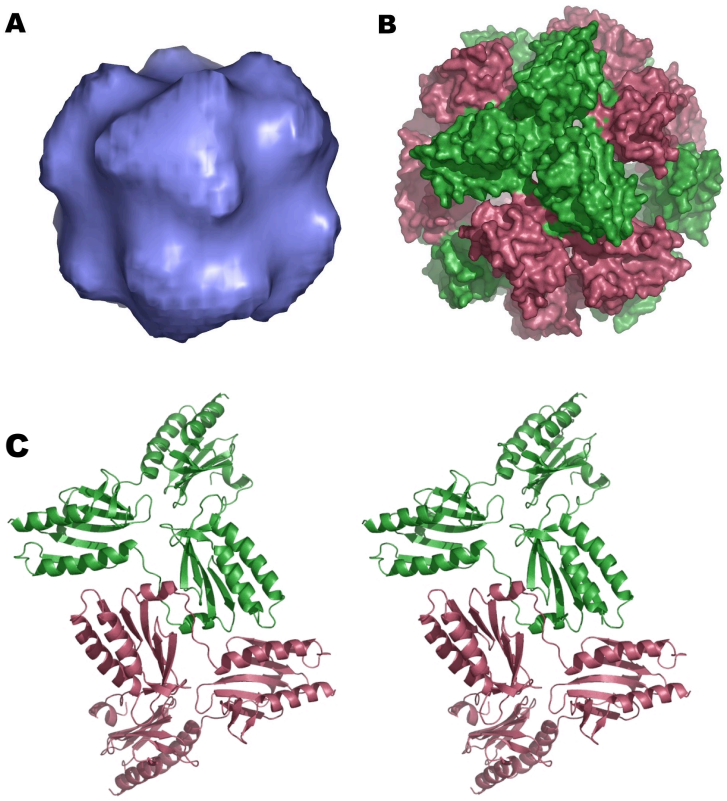

Karlberg et al, Fig. 4

Supporting Online Material

Materials and Methods

Protein preparation and crystallization

The mutant Y73A frataxin from *S. cerevisiae* was recombinantly expressed in *E. coli* and purified with a modification of the procedure described previously for human frataxin (*1*). Bacterial lysate (~25 ml at 26 mg/ml total protein) was applied to a Macro-Prep DEAE column (16 mm x 50 cm) (Bio-Rad), and protein was eluted with a 1-L linear gradient, from 50 to 525 mM NaCl, in 20 mM Tris-HCl, pH 8.0 at a flow rate of 10 ml/min. Most Y73A frataxin was eluted in two separate pools, a low-salt pool (300-380 mM NaCl) containing α_3, and a high-salt pool (440-510 mM) containing α_{24}. Each DEAE pool was diluted to 600 ml, loaded onto a Macro-Prep High Q column (Bioscale MT20) (Bio-Rad), and the protein eluted with a 500 ml linear NaCl gradient as described above at a flow rate of 5 ml/min. Two High Q pools were obtained, α_{24} (~410-510 mM NaCl) and α_3 (~200-290 mM NaCl). Each pool was concentrated to 1 ml, loaded onto a Sephacryl 300 column (16 mm x 60 cm) (Amersham-Biosciences), and eluted with 120 ml of 10 mM HEPES-KOH, pH 7.3, 100 mM NaCl, at a flow rate of 0.4 ml/min. Fractions containing α_3 or α_{24} were pooled and applied to a Mono Q HR5/5 column (Amersham-Biosciences) and eluted with a linear gradient, from 100 to 450 mM NaCl, at flow rate of 1ml/min. Fractions containing α_3 (~200-250 mM NaCl) or α_{24} (~280-310 mM NaCl) were concentrated and buffer exchanged to 10 mM HEPES-KOH, pH 7.3.

Crystallization conditions for trimeric frataxin were found by use of commercially available screens (Hampton Research) and by further optimizing promising conditions.

Crystals were grown by vapor diffusion in a hanging drop at 15°C. Crystallization drops were made by mixing 3 μL of a protein solution at a concentration of 7 mg/ml in 10 mM KOH-HEPES, pH 7.3, with 3 μL of a reservoir solution containing 0.1 M Bis-Tris (pH 5.5), 2.0 M Ammonium sulphate, and 4% (v/v) γ-Butyrolactone. Crystals appeared after 5 days. The best crystals had dimensions of approximately 0.15 mm × 0.15 mm × 0.15 mm. Two different crystal forms (space groups R32 and $I2_13$) were obtained. A cobalt(II)-derivative was made by adding crystalline $CoCl_2$ directly into a drop with frataxin crystals to a concentration of about 0.4 mM. The crystals were then set to soak for 15 minutes. Longer soaking time resulted in poor quality of diffraction. Iron-loading of frataxin trimer was achieved by incubating the purified oligomer with ferrous iron at a molar ratio of 2 iron atoms per monomer for 2 h at 30°C, followed by isolation of iron-loaded trimer by size-exclusion chromatography. Crystals in space-group $I2_13$ were obtained in the same manner as for the metal-free trimer.

Data collection and structure determination

For data collection, 25% Glycerol was used as cryoprotectant, crystals were mounted on a rayon loop and flash-cooled directly in a stream of boiled-off nitrogen.

Two native datasets to 2.8 Å (R32) and 3.0 Å ($I2_13$) resolution respectively and a cobalt(II)-soaked derivative to 3.7 Å ($I2_13$), were collected using a MAR Research CCD detector at MAX II synchrotron laboratory stations I711 and I911-2 in Lund, Sweden (*2, 3*). A dataset of the iron-loaded trimer was collected using an ADSC CCD detector at beamline ID23-1, ESRF synchrotron facility in Grenoble, France, to a resolution of 3.6 Å ($I2_13$). All datasets were processed with the XDS package (*4*). The structure was solved

by molecular replacement using a combination of the solved crystal structure of the monomeric human frataxin (*5*) and the bacterial frataxin CyaY from *E. coli* (*6*) as a search probe with the program Phaser (*7*). The model was then built using the graphical program O (*8*) and refined with CNS (*9*). The progress of refinement was followed by decreasing R and R_{free} values. Data collection and refinement statistics are shown in Table S1. Coordinates have been deposited in the Protein Data Bank with accession number 2FQL.

The unprocessed frataxin from *S. cerevisiae* contains 174 amino acids. Upon transport into mitochondria it is cleaved to its mature form in two sequential steps (*10*). The resulting polypeptide, which was used in this study, consists of 123 residues (52-174). Of these the first nine (52-60) and the last two amino acids (173-174) appeared to be disordered in the electron density maps and, thus, could not be modeled.

As noted above, frataxin trimer crystallizes in two different space groups, $I2_13$ and R32. While the general appearance of the structures is essentially the same, the packing of the trimers within the crystal lattice was different. In space group $I2_13$ two monomers from neighboring trimers pack with their β-sheets facing each other, while in R32 the β-sheet from one trimer faces the helical side of a neighboring trimer. In both space-groups the N-terminal extension is responsible for the interactions within the crystal lattice, being sandwiched between the structural elements. It has slightly different conformations in the two space-groups, which demonstrates its flexibility and ability to adopt to different packing without disrupting the trimer structure.

Electrostatic potential calculations

Calculations of the electrostatic potential in the central pore of the frataxin trimer were performed by solving the Poisson equation with the program MEAD (macroscopic electrostatic with atomic detail) (*11, 12*). The protein was described as a volume of a dielectric constant of 4 dissolved in water with the dielectric constant of 80. All atoms in the protein were assigned a partial charge, taken from the Amber 2003 force field (*13, 14*). The Asp and Glu residues were assumed to be negatively charged and the Lys and Arg residues positively charged. Based on the hydrogen-bond pattern, the surroundings, and the solvent exposure, we decided to let His-74, 83, and 106 to be doubly protonated and therefore positively charged, whereas His-95 was protonated on the $N^{\varepsilon 2}$ atom. Hydrogen atoms were added and optimised by Amber 8 (*13*) before the MEAD calculations. All atoms were assigned PARSE radii (*15*). The electrostatic potential was calculated along the threefold symmetry axis using a 0.5 Å grid with at least twice the size of the protein (251^3 grid points). The calculations were run at 300 K. The result is presented as the interaction energy with a +2 charged ion.

EM data collection and image processing

Protein solution (2 µl of 0.2 mg/ml) was applied to carbon coated, glow discharged copper grids (400-mesh, Electron Microscopy Sciences, USA) and allowed to adsorb for 1 minute. Excess solution was blotted off and the grids were subsequently stained with either 1% uranyl acetate in water (2 µl for 10 seconds) or 1% phosphor tungsten acid in 20 mM phosphate buffer pH 6.9 (2 µl for 1 minute). Images were

acquired using a Philips CM120 equipped with a Gatan GIF 100 energy filter and Gatan 791 CCD camera (1024×1024 pixels) at a magnification of 52400× (sampling distance 4.67 Å).

The image processing was performed with a Eman software package (*16*) applying octahedral point group symmetry. The iterative classification procedure converged after eight cycles of reclassifications and 4,000 particles out of the 5,400 were used for calculating the final reconstruction. The resolution of the frataxin oligomer was determined to 19 Å according to the 0.5 Fourier shell correlation criteria. Strict damping of the FSC-curve in high-resolution shells was observed, which together with the comparison between class averages and projections is an indication that the envelope of the classification process is not limiting.

The docking of the X-ray structure into the EM-reconstruction was done in Chimera (*17*). The modification of the trimeric x-ray structure was done in O (*8*). The final reconstruction of the 24-subunit oligomer was evaluated by comparing class averages with projection images in the same angular orientation of the interpolated model (Fig. S4A, B). The image pairs revealed the same structural features, an indication of the reconstruction being in a global minimum, rather than trapped in a local one. An initial reconstruction was performed without any symmetry. The result reveals a cubic shape of the molecule, vindicating our use of octahedral symmetry (result not shown). Several independent reconstructions aligning on either point group symmetry or varying reference models gave similar results. To induce a better fit to the EM model the monomer had to be tilted by an angle of about 12° compared to its position in the X-ray

model. The tilt did not introduce any notable changes in the internal interactions within the trimeric structure and the size of the channel was conserved.

Supporting References

1. P. Cavadini, H. A. O'Neill, O. Benada, G. Isaya, *Hum Mol Genet* **33**, 217 (2002).
2. Y. Cerenius *et al.*, *J. Synchr. Rad.* **7**, 203 (2000).
3. C. B. Mammen, T. Ursby, M. Thunnissen, J. Als-Nielsen, *AIP Conference Proceedings* **705**, 808 (2004).
4. W. Kabsch, *J. Appl. Crystallogr.* **26**, 795 (1993).
5. S. Dhe-Paganon, R. Shigeta, Y. I. Chi, M. Ristow, S. E. Shoelson, *J Biol Chem* **275**, 30753 (2000).
6. S. J. Cho *et al.*, *Proc Natl Acad Sci U S A* **97**, 8932 (2000).
7. A. J. McCoy, R. W. Grosse-Kunstleve, L. C. Storoni, R. J. Read, *Acta Crystallogr D Biol Crystallogr* **61**, 458 (2005).
8. T. A. Jones, J. Y. Zou, S. W. Cowan, Kjeldgaard, *Acta Crystallogr A* **47 (Pt 2)**, 110 (1991).
9. A. T. Brunger *et al.*, *Acta Crystallogr D Biol Crystallogr* **54 (Pt 5)**, 905 (1998).
10. S. S. Branda *et al.*, *J Biol Chem* **274**, 22763 (1999).
11. D. Bashford, in *Scientific computing in object-oriented parallel environments* Y. Ishikawa, R. R. Oldehoeft, J. V. W. Reynders, M. Tholburn, Eds. (Berlin: Springer, 1997) pp. 233-240.
12. D. Bashford, K. Gerwert, *J Mol Biol* **224**, 473 (1992).
13. D. A. Case *et al.*, *University of California San Francisco* (2004).
14. W. D. Cornell *et al.*, *J. Am. Chem. Soc.* **117**, 5179 (1995).
15. D. Sitkoff, K. A. Sharp, B. Honig, *J. Phys. Chem.* **98**, 1978 (1994).
16. S. J. Ludtke, P. R. Baldwin, W. Chiu, *J Struct Biol* **128**, 82 (1999).

17. E. F. Pettersen *et al.*, *J Comput Chem* **25**, 1605 (2004).

18. Y. He *et al.*, *Biochemistry* **43**, 16254 (2004).

19. A. C. Rosenzweig *et al.*, *Structure* **7**, 605 (1999).

20. H. K. Song, S. B. Mulrooney, R. Huber, R. P. Hausinger, *J Biol Chem* **276**, 49359 (2001).

21. S. Adinolfi *et al.*, *Biochemistry* **43**, 6511 (2004).

22. G. J. Barton, *Comput Appl Biosci* **9**, 729 (1993).

23. V. Campuzano *et al.*, *Science* **271**, 1423 (1996).

24. All figures except S2C, S3 and S4 were generated with the PyMOL Molecular Graphics System (2002) Delano Scientific, San Carlos, CA, U.S.A.

Supporting Figure Legends

Fig. S1. Superposition of the structure of yeast frataxin monomer, as found within the trimer (green), with (**A**) the NMR structure of yeast frataxin monomer (purple) (*18*) and (**B**) X-ray structure of human frataxin monomer (yellow) (*5*). The overall structure of frataxin within the trimer is similar to the solution structure of yeast frataxin (*18*) (**A**), as well as to the structure of human frataxin (**B**) and *E. coli* CyaY (not shown) (*5, 6*). Interestingly, a similar fold is also found in two other metallochaperones, Atx1 copper chaperone (*19*) and the C-terminal domain of UreE nickel chaperone (*20*), which suggests evolutionary relationships between metal trafficking proteins. However, in (**A**) striking differences are observed at the C-terminal helix α3, the loops between the β-strands and the N-terminal part of the structure, including helix α2. This helix is about two turns longer in the NMR structure. It generally appears that the solution structure has a much more 'loose' packing, compared to the crystal structure. This can probably be related to the observed low thermo-stability of yeast frataxin in solution, when compared to its human counterpart (*21*). The difference in conformation is most probably induced by trimer formation. In (**B**) large differences are also observed at the N-terminus of helix α2, which contains two additional turns. Thus, it seems that the formation of the trimer results in unfolding of this helix.

Fig. S2. Stabilization of the trimer by the N-terminal extension. (**A**) At the base, the conformation of the N-terminal extension is stabilized by an extensive network of hydrogen bonds between main chain carbonyls of A72, H74 and E75 with amide groups of H74, E76 and D78, respectively, and between side chains of H74, E76 and D78, with

side chains of D79, R141 and K123, respectively. (**B**) Interactions of helix α1 with the β-sheet include residues P62, E64, V65 and L68 from α1, and residues T110, E112, T118 and V120 from the β-sheet. Hydrophobic residues P62, V65 and L68 in the N-terminal extension are directly packed against residues T110 and T118. There is only one hydrogen bond formed between the side chain of T118 and the carbonyl oxygen of E64. (**C**) Calculated metal binding energy for the two different conformations of the loops at the exit of the channel (blue and red for the first and second conformation, respectively). The predicted optimial position of the metal in the two conformations differes by about 3.5 Å.

Fig. S3. Alignment of the amino acid sequences of frataxin from yeast, human, mouse and drosophila with the bacterial CyaY frataxin analogues from *S. typhimurium*, *E. coli* and *P. aeruginosa*. Residues conserved only in eukaryotic or bacterial sequences are marked in green and blue, respectively. Invariant residues are marked in red. The position of secondary structure elements is shown along the sequence. The overall sequence identity is 40% between the yeast and human sequences and 28% between the 106 overlapping residues (68-174) of the yeast and *E. coli* sequences. Figure generated with Alscript (*22*).

Fig. S4. (**A**) EM images of the 24-subunit oligomer in 1% uranyl acetate negative stain on the recorded micrograph. (**B**) A comparison between projection images of the reconstructed model (to the left) and the class averages (to the right).

Fig. S5. Position of pathogenic frataxin point mutations. Defects in frataxin are linked with the neurodegenerative disease Friedreich ataxia (FRDA) (*23*). Most FRDA patients carry large repeat expansions in the first intron of the frataxin gene that hamper transcription causing a severe reduction in the levels of frataxin protein. About 4% FRDA patients carry an expansion in one allele and a point mutation in the other allele. While the majority of FRDA point mutations affect the hydrophobic core of the structure (L84S, I130F, L132P, W149G, L158H, L158F, yeast numbering), 4 mutations appear to destabilize the formation of the trimeric complex. These include G107V, W131R, R141C (G130V, W155R and R165C, human numbering) and D122Y at a position which corresponds to P100 in yeast. P100 is located in the loop between helix α2 and strand β1 at the tip of the monomer close to the surface against which helix α1 is packed. G107 is located in a loop between strands β1 and β2. Its carbonyl oxygen makes a hydrogen bond to the amide group of K123, thus contributing to the stabilization of the conformation of the regions between K123-I130. K123 is also involved in interactions with the N-terminal extension through a hydrogen bond to D78 (Fig. S2A). Moreover, W131, which is exposed to the surface of the central β-sheet, is involved in interaction with the N-terminal extension. Another mutation, R141C, in human frataxin will disrupt a hydrogen bond to the carbonyl of P125, which may affect the conformation of the loop at the channel exit.

Table S1: Data collection and refinement statistics.

Data collection	**Native I**	**Native II**	**Fe(II)-loaded**	**Co(II)-soaked**
Beamline	I911-2	I711	ID23-1	I711
Space group	$I2_13$	R32	$I2_13$	$I2_13$
Wavelength (Å)	1.0516	1.0863	0.97625	1.0630
Cell dimensions, a, b, c (Å)	121.22, 121.22, 121.22	148.90, 148.90, 182.97	123.80, 123.80, 123.80	121.52, 121.52, 121.52
Resolution range (Å)	20-3.0 (3.2-3.0)	20-2.8 (3.0-2.8)	25-3.6 (3.8-3.6)	20-3.7 (3.9-3.7)
Completeness (%)	98.3 (94.7)	94.1 (97.9)	99.6 (99.4)	99.4 (99.0)
I/SIGMA(I) > 3 (%)	86.3 (61.1)	90.1 (73.3)	95.6 (83.2)	88.9 (68.3)
Multiplicity	11.6 (11.9)	11.8 (12.2)	22.8 (22.4)	9.7 (9.7)
R_{merge}[a]	0.051 (0.22)	0.054 (0.17)	0.036 (0.11)	0.075 (0.13)
Solvent content (%)	77.2	74.0	78.6	77.4
Refinement				
R_{cryst} (R_{free})[b]	0.230 (0.276)			
R.m.s.d.[c]				
Bond distances (Å)	0.011			
Bond angles (deg.)	1.9			

[a]$R_{merge} = \Sigma|I_i - \langle I \rangle|/\Sigma I$, where I_i is an individual intensity measurement and $\langle I \rangle$ is the average intensity for this reflection.

[b]$R_{cryst} = \Sigma|F_{obs} - F_{calc}|/\Sigma F_{obs}$, where F_{obs} and F_{calc} are the observed and calculated structure factor amplitudes, respectively. R_{free} is the same as R_{cryst} but calculated on 5% of the data excluded from refinement.

[c]Root-mean-square deviations of the parameters from their ideal values.

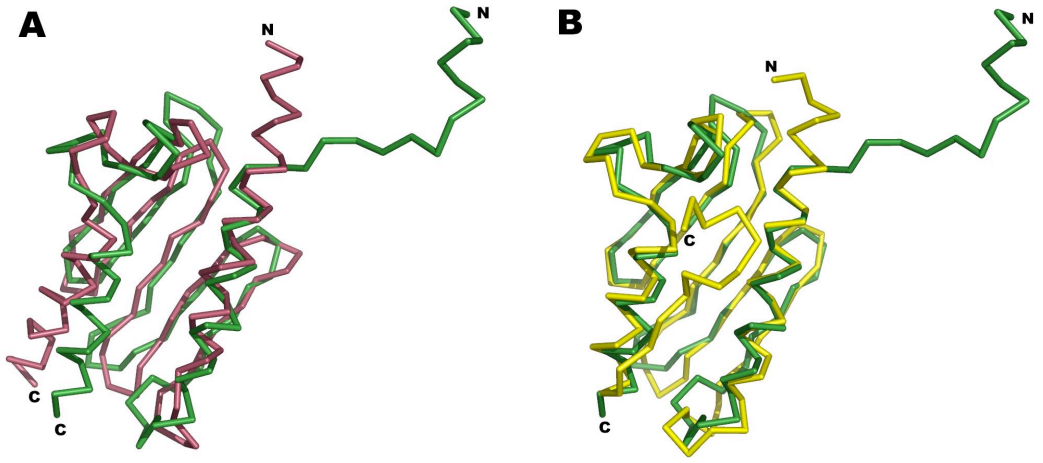

Karlberg et al, Fig. S1

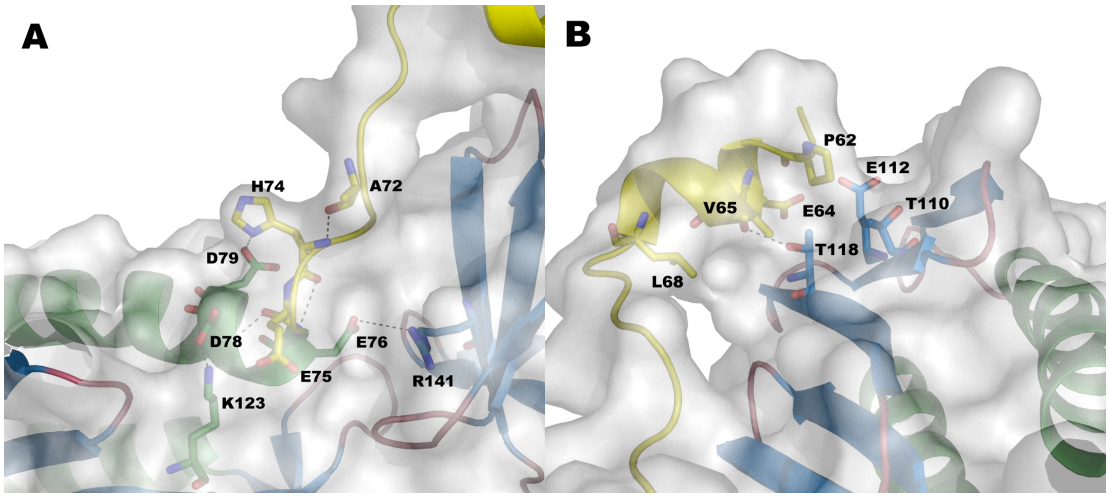

+ ULFS BILD

Karlberg et al, Fig. S2

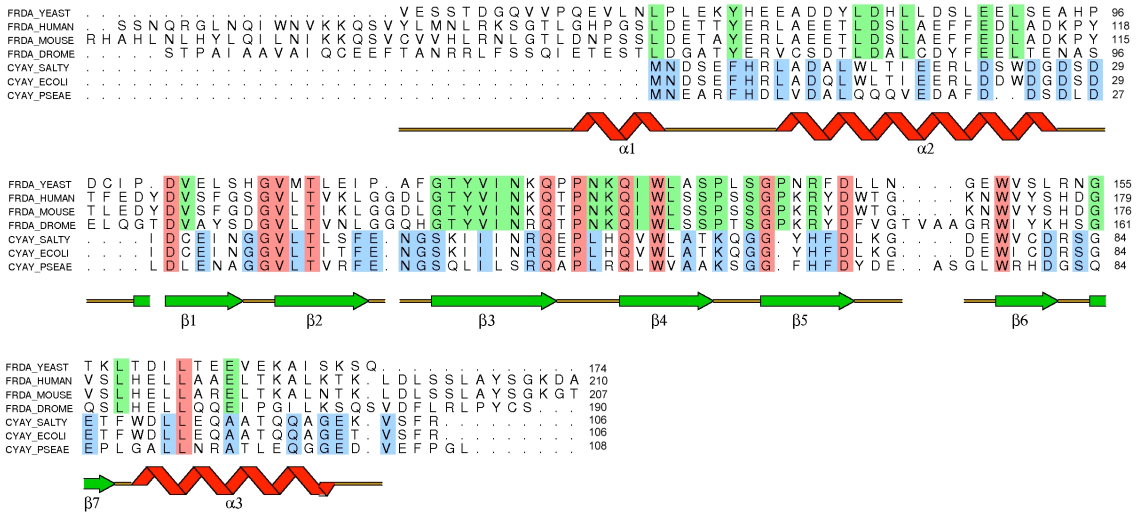

Karlberg et al, Fig. S3

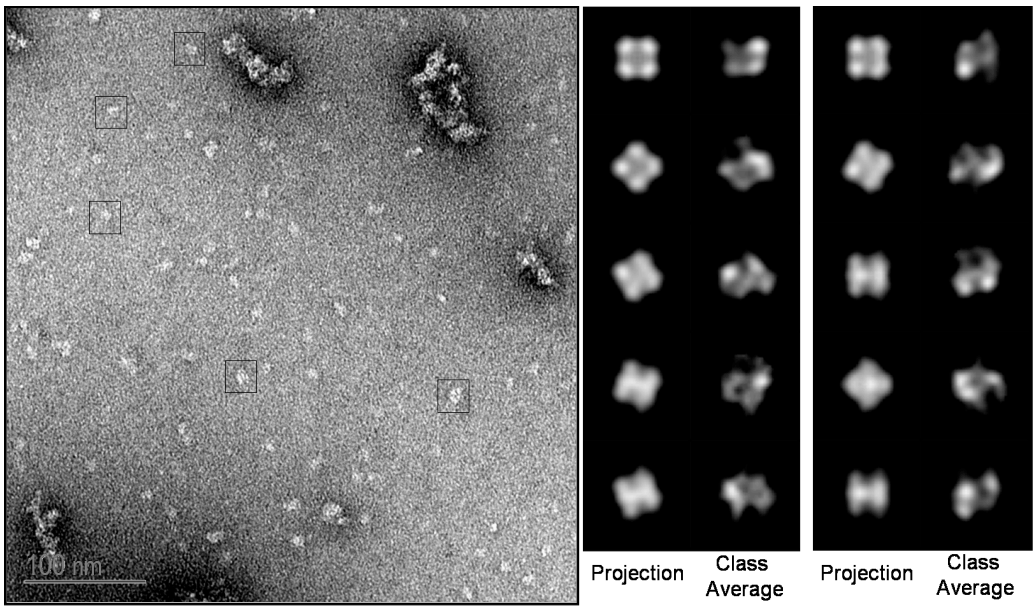

Karlberg et al, Fig. S4

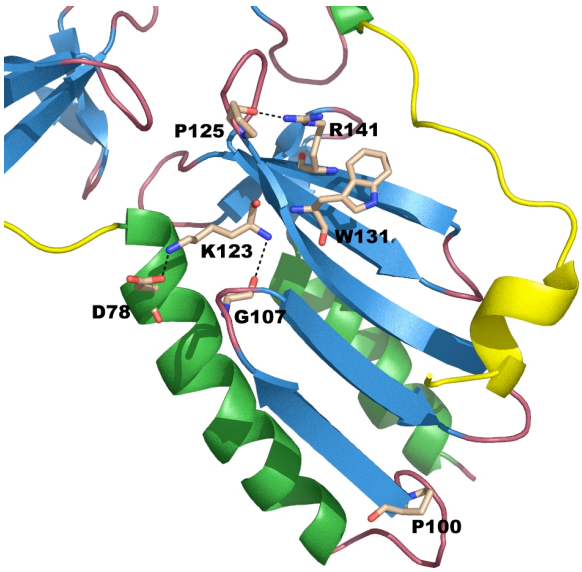

Karlberg et al, Fig. S5